Observation of Nematic Texture in a Diblock Copolymer Melt

Ferass M. Abuzaina,[†] Bruce A. Garetz,*[,†] Amish J. Patel,[‡] Maurice C. Newstein,[†] Samuel P. Gido,[§] Xiaochuan Hu,[§] and Nitash P. Balsara*[,‡]

Othmer Department of Chemical & Biological Sciences & Engineering and Department of Electrical Engineering, Polytechnic University, Brooklyn, New York 11201, Department of Polymer Science and Engineering, University of Massachusetts, Amherst, Massachusetts 01013, and Department of Chemical Engineering and Materials Sciences Division, Lawrence Berkeley National Laboratory, University of California, Berkeley, California 94720

Received November 11, 2005; Revised Manuscript Received February 13, 2006

ABSTRACT: We have observed nematic textures in polarized optical microscopy and "plus" (+) patterns in depolarized light scattering (four lobes parallel to polarizer/analyzer axes) from a deeply quenched diblock copolymer melt with a cylindrical microstructure. Both of these features are similar to those found in nematic liquid crystalline polymers. In contrast, this same polymer sample exhibits a more conventional grain structure at shallower quench depths, characterized by an "X" pattern in depolarized light scattering (lobes at 45° to polarizer/analyzer axes). A theoretical model is used to analyze the "plus" scattering patterns obtained from nematic textures in the single scattering limit. This model is used to quantify the nature of local correlations in our deeply quenched block copolymer melt. We show that the nematic texture is easy to align by shear flow while the granular structure is not.

Introduction

Block copolymers can spontaneously self-assemble into a variety of periodic microphase-separated, nanometer-sized ordered domains, such as spheres, cylinders, gyroids, and lamellae.[1−6] The long range order of these domains in bulk samples and thin films has been the subject of many theoretical and experimental studies.[7−23] In particular, our group has been using depolarized light scattering to investigate the relationship between the optical properties and the grain structure of ordered block copolymers.[24−30] Our earliest studies considered samples composed of randomly oriented "ideal" grains: uncorrelated grains whose optic axes are uncorrelated with their shapes.[24,25] More complex systems have included samples containing ellipsoidal grains whose optic axes lie along their shape axes[26,27] and samples consisting of correlated clusters of ellipsoidal grains.[28] Recently, we have developed a model that assumes an anisotropic orientation distribution of ellipsoidal grains in a sample under shear flow.[29,30]

In this paper we use depolarized light scattering (DPLS) and polarized optical microscopy (POM) to investigate a polystyrene−polyisoprene (SI) diblock copolymer that exhibits a nematic texture when annealed at a relatively large quench depth. The corresponding DPLS patterns exhibit 4-fold symmetry where the lobes of the patterns are oriented along the polarizer/analyzer axes. We thus refer to these patterns as "plus" patterns hereafter. The plus pattern has not been previously observed in block copolymers. An important goal of this work is to develop a model for quantitative analysis of the plus DPLS pattern in terms of the size, shape, and relative arrangement of the local coherently ordered regions.

* To whom correspondence should be addressed.
[†] Othmer Department of Chemical & Biological Sciences & Engineering and Department of Electrical Engineering, Polytechnic University.
[‡] Department of Chemical Engineering, and Materials Sciences Division, Lawrence Berkeley National Laboratory, University of California, Berkeley.
[§] Department of Polymer Science and Engineering, University of Massachusetts.

Polarized optical microscopy (POM) has been used by Chastek and Lodge to determine grain shapes and growth kinetics in solutions of cylindrical SI diblock copolymers.[23] This technique is particularly well suited to shallow quenches in which the nucleation density is low, so that grains can grow to sizes of hundreds of micrometers without impinging on neighboring grains; such sizes are well within the resolution limits of optical microscopy.

POM has also been widely recognized as one of the most powerful methods to investigate liquid crystalline substances.[31,32] Not only can one identify if the substance is a liquid crystal but one can also distinguish the type of liquid crystal to some extent. Nematic liquid crystalline thin films held between untreated glass plates often orient with their directors parallel to the substrates. If this orientation is not homogeneous, but varies slowly in the plane of the substrate, so-called *Schlieren* textures are observed between crossed polarizers.[31]

Nematic textures have been reported in the literature as a signature of both rigid and semiflexible main chain liquid crystalline polymers[33] and also for cholesteric,[34] lyotropic,[35] and thermotropic[36−39] nematic polymers. They have also been reported for micelles.[40] To our knowledge, this is the first report of a nematic texture arising in a bulk diblock copolymer melt.

Wang and Hashimoto showed that SI block copolymers with lamellar or cylindrical microdomains in bulk could form a smectic or a columnar lyotropic liquid crystal phase.[41,42] Their reports were the first to show clear optical microscopy evidence of micrometer-sized liquid-crystalline textures in bulk block copolymers, when prepared by evaporation from solution. Prior to that work, there were a few reports, based on observations of microdomain morphology under transmission electron microscopy (TEM), showing evidence that some local defects, similar to those formed in liquid crystals, have been visualized in the bulk block copolymers.[43,44] Recently, using scanning force microscopy (SFM), Kramer and co-workers have observed a "nematic" phase in monolayers of a cylindrical diblock copolymer of polystyrene and poly(2-vinylpyridine), where the nematic

10.1021/ma052413w CCC: $33.50
Published on Web 04/01/2006

director is normal to the cylinder axis, in the plane of the monolayer.[16]

Theoretical Background

There are no satisfactory models in the literature that can accurately describe typical observed "plus" depolarized scattering patterns obtained from nematic liquid crystalline polymers. Two early attempts to develop such models were by Hashimoto and Stein[36] and by Greco.[45] In the former case, the basic scattering unit was assumed to be an isolated disk with a single disclination at the center. The agreement between this model and experimental patterns was poor, suggesting that two-, three-, and many-body interactions among neighboring disks were essential. Greco assumed that the basic scattering unit was a disk that enclosed a dipole consisting of a pair of $S = \pm 1/2$ disclinations. The scattering patterns obtained from this model are in qualitative agreement with the plus pattern. We have expanded on these ideas in developing the following two-grain model.

Two-Grain Model

The standard nematic structure comprises a set of directors whose orientation changes continuously as they terminate in closely spaced pairs of $S = \pm 1/2$ disclinations, as shown in Figure 1a. We have highlighted two crescent-shaped regions in this figure where the director makes an angle of $\pm 45°$ to the line connecting the two disclinations. We will approximate this complex structure by two parallel ellipsoidal grains of the same shape, with each grain's optic axis at 45° to its shape axis in such a way that the two optic axes are at right angles, also shown in Figure 1a. The two-grain system, along with associated length parameters, is shown in Figure 1b. This model provides a coherent scattering unit in which the director rotates through 90°, somewhat reminiscent of the scattering unit employed by Greco.[45] This two-grain model is substantially different from the three-grain models we have used in the past for fitting "clover-leaf" X-type scattering patterns. In the three-grain models, the optic axis is always parallel to the shape axis of each ellipsoidal grain,[28] whereas in the new two-grain model, the optic axis makes an angle of 45° to the shape axis of each grain.

A diagram illustrating the vectors and angles used to describe the scattering geometry is provided in Figure 2. The unit vector in the direction of the common grain axis, **g**, has the Cartesian coordinates

$$\mathbf{g} = \{\sin\theta_g \sin\mu_g, \sin\theta_g \cos\mu_g, \cos\theta_g\} \qquad (1)$$

where θ_g and μ_g are the polar and azimuthal angles of **g** with respect to the laboratory $x-y-z$ coordinate system. Let $\{\mathbf{a}_\xi, \mathbf{a}_\eta, \mathbf{g}\}$ be an orthonormal set of unit vectors. We can take $\mathbf{a}_\xi$ to be perpendicular to $\mathbf{a}_z$ and **g**, where $\mathbf{a}_z$ is a unit vector in the z direction:

$$\mathbf{a}_\xi = \mathbf{a}_z \times \mathbf{g}/|\mathbf{a}_z \times \mathbf{g}|$$
$$\mathbf{a}_\eta = \mathbf{g} \times \mathbf{a}_\xi \qquad (2)$$

Take the optic axis of grain A to be at 45° to the g axis and at the azimuthal angle σ measured from the ξ axis in the ξ-η plane. Then the optic axis of grain A, $\mathbf{o}_A$ is given by

$$\mathbf{o}_A = \frac{1}{\sqrt{2}}(\mathbf{a}_\xi \cos\sigma + \mathbf{a}_\eta \sin\sigma + \mathbf{g}) \qquad (3)$$

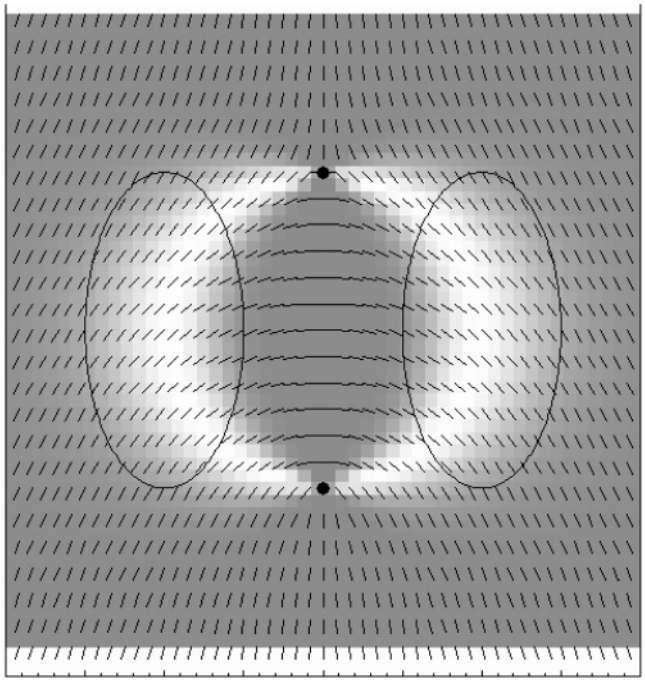

a

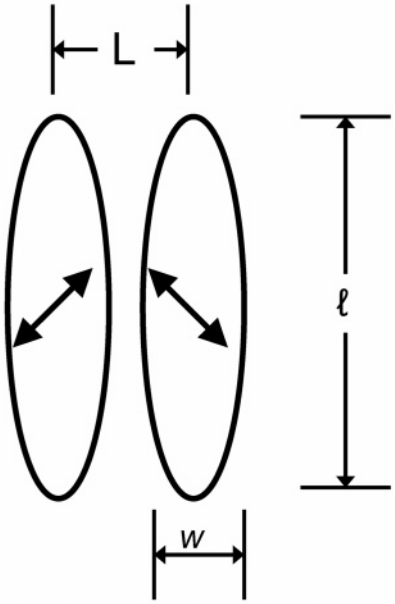

b

Figure 1. (a) Nematic director field in the vicinity of an $S = \pm 1/2$ disclination dipole, highlighting regions where the director makes an angle of about $\pm 45°$ to the dipole direction. (b) Schematic of the two-grain model. Two ellipsoidal grains have parallel shape axes, but optic axes at 45° to their respective shape axes, and 90° to each other.

For our assumed geometric configuration, the optic axis of grain B, $\mathbf{o}_B$, is given by

$$\mathbf{o}_B = \frac{1}{\sqrt{2}}(-\mathbf{a}_\xi \cos\sigma - \mathbf{a}_\eta \sin\sigma + \mathbf{g}) \qquad (4)$$

By inspection we see that the two vectors $\mathbf{o}_A$ and $\mathbf{o}_B$ are orthonormal. We take the displacement vector, **L**, from the center of grain A to the center of grain B to be parallel to $\mathbf{o}_A - \mathbf{o}_B$:

$$\mathbf{L} = (\mathbf{a}_\xi \cos\sigma + \mathbf{a}_\eta \sin\sigma)L \qquad (5)$$

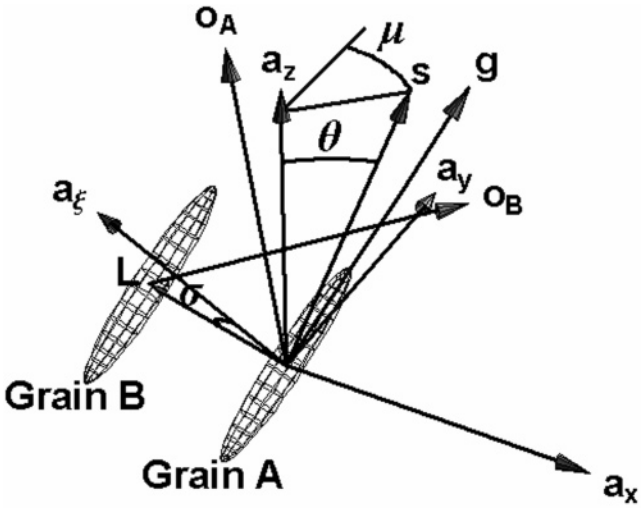

Figure 2. Diagram illustrating vectors and angles used in the light scattering model. The vectors $\mathbf{a}_x$, $\mathbf{a}_y$, and $\mathbf{a}_z$ are the orthonormal basis vectors in the laboratory frame. $\mathbf{g}$ is the unit vector along the grain axis of grain A. The grain axis of grain B is parallel to that of grain A. $\mathbf{L}$ is the vector, perpendicular to $\mathbf{g}$, from the center of grain A to that of grain B. $\mathbf{o}_A$ is the optic axis of grain A and is at 45° to the grain axis $\mathbf{g}$. $\mathbf{o}_B$ is the optic axis of grain B, also at 45° to $\mathbf{g}$, but at such an orientation that $\mathbf{o}_A$ and $\mathbf{o}_B$ are perpendicular. $\mathbf{a}_\xi$ is a vector perpendicular to $\mathbf{g}$ chosen as a reference for the measurement of the spin angle σ about the grain axis of grain A. $\mathbf{a}_\xi$ and $\mathbf{L}$ lie in the plane perpendicular to $\mathbf{g}$, and the angle between them is σ. The incident beam travels in the direction of $\mathbf{a}_z$, and $\mathbf{s}$ is a unit vector in a scattered beam direction, making a polar angle θ with respect to $\mathbf{a}_z$ and an azimuthal angle μ, measured from $\mathbf{a}_y$, in the $\{x, y\}$ plane.

L is the magnitude of $\mathbf{L}$. The y-component of the field at the far point $\mathbf{r}_{ff}$ scattered by the grain pair is[25]

$$E = \frac{C}{r_{ff}} E_0 e^{-ikr_{ff}} \{\mathbf{a}_x \cdot \mathbf{o}_A \mathbf{o}_A \cdot \mathbf{a}_y F_A(\mathbf{q}) + \mathbf{a}_x \cdot \mathbf{o}_B \mathbf{o}_B \cdot \mathbf{a}_y F_B(\mathbf{q})\} \quad (6)$$

where $\mathbf{q}$ is the scattering vector given by

$$\mathbf{q} = k(\mathbf{s} - \mathbf{a}_z) \quad (7)$$

and $\mathbf{s}$ is a unit vector directed from the grain pair toward the far-field point $\mathbf{r}_{ff}$. The symbol $\mathbf{o}_A\mathbf{o}_B$ represents a dyadic tensor with the ijth element equal to $(\mathbf{o}_A)_i(\mathbf{o}_B)_j$. The scattering vector will be approximated by its paraxial limit:

$$\mathbf{q} \approx k\theta(\sin\mu, \cos\mu, 0) \quad (8)$$

This approximation leads to an expression for the scattered intensity correct to order θ^3. The angles θ and μ are the polar and azimuthal angles of the scattered field direction, $\mathbf{s}$. E_0 is the field amplitude of the incident plane wave, the constant C is given by $C = n(n_e - n_o)k^2/2\pi$, and k is the wavevector amplitude equal to $2\pi/\lambda$, where λ is the wavelength of the incident light. The refractive index of a grain for light polarized parallel or perpendicular to the grain optic axis is given by n_e or n_o, respectively, and n is the average refractive index. The functions $F_A(\mathbf{q})$ and $F_B(\mathbf{q})$ are Fourier transforms of the corresponding shape functions $f_A(\mathbf{r}')$ and $f_B(\mathbf{r}')$, where $f(\mathbf{r}')$ is equal to 1 if $\mathbf{r}'$ lies in the grain and 0 otherwise.

$$F(\mathbf{q}) = \int d\mathbf{r}' \, e^{-i\mathbf{q}\cdot\mathbf{r}'} f(\mathbf{r}') \quad (9)$$

Evaluation of Shape Factor Transforms

To facilitate later evaluations we approximate the grain shape functions by Gaussian forms whose contours of constant value are ellipsoids of revolution about the grain axis:

$$f_A(\mathbf{r}) = \exp\left(-\left(\frac{\mathbf{g}\cdot\mathbf{r}}{l}\right)^2\right) \exp\left(-\frac{(\mathbf{a}_\xi\cdot\mathbf{r})^2 + (\mathbf{a}_\eta\cdot\mathbf{r})^2}{w^2}\right) \quad (10)$$

$$f_B(\mathbf{r}) = \exp\left(-\left(\frac{\mathbf{q}\cdot(\mathbf{r}-\mathbf{L})}{l}\right)^2\right) \exp\left(-\frac{(\mathbf{a}_\xi\cdot(\mathbf{r}-\mathbf{L}))^2 + (\mathbf{a}_\eta\cdot(\mathbf{r}-\mathbf{L}))^2}{w^2}\right) \quad (11)$$

where l and w are grain length parameters parallel and perpendicular to the ellipsoid rotation axis, respectively; we get for their transforms[25]

$$F_A(\mathbf{q}) = (\pi^{3/2}/w^2) \exp\left(-\frac{1}{4}(l^2 - w^2)(\mathbf{q}\cdot\mathbf{g})^2\right) \exp\left(-\frac{1}{4}w^2q^2\right) \quad (12)$$

$$F_B(\mathbf{q}) = \exp(-i\mathbf{q}\cdot\mathbf{L})F_A(\mathbf{q}) \quad (13)$$

$$\mathbf{q}\cdot\mathbf{g} = q\cos(\mu - \mu_g)\sin\theta_g \quad (14)$$

$$\mathbf{q}\cdot\mathbf{L} = qL\,(-\cos\sigma\sin(\mu - \mu_g) + \cos\theta_g\cos(\mu - \mu_g)\sin\sigma) \quad (15)$$

The power scattered by the AB grain pair, I_{AB}, is proportional to $|E|^2$. Aside from multiplicative constants, we have

$$I_{AB} = (\mathbf{a}_x\cdot\mathbf{o}_A\mathbf{o}_A\cdot\mathbf{a}_y)^2|F_A(\mathbf{q})|^2 + (\mathbf{a}_x\cdot\mathbf{o}_B\mathbf{o}_B\cdot\mathbf{a}_y)^2|F_B(\mathbf{q})|^2 + 2(\mathbf{a}_x\cdot\mathbf{o}_A\mathbf{o}_A\cdot\mathbf{a}_y)(\mathbf{a}_x\cdot\mathbf{o}_B\mathbf{o}_B\cdot\mathbf{a}_y)\mathrm{Re}(F_A(\mathbf{q})F_B(\mathbf{q})^*) \quad (16)$$

Neglecting interference between different grain pairs, which leads to a high spatial frequency speckle pattern, the power scattered by the ensemble of grain pairs is proportional to the average of I_{AB} over the orientation angles, θ_g and μ_g, and the spin angle σ. Aside from constant multiplicative factors, this is given by

$$\langle I_{AB}\rangle = \int_0^\pi \sin\theta_g \, d\theta_g \int_0^{2\pi} d\mu_g \int_0^{2\pi} d\sigma \, I_{AB} \quad (17)$$

Since the μ_g integration is over the full angular range from 0 to 2π, we may eliminate μ from the F_A and F_B terms by making the substitution $\mu_g \rightarrow \mu_g + \mu$, and the defining equations can be written

$$\langle I_{AB}\rangle = \int_0^\pi \sin\theta_g \, d\theta_g \int_0^{2\pi} d\mu_g \int_0^{2\pi} d\sigma \sin\theta_g F_A{}^2((xaay^2 + xbby^2) + 2\,(xaay\,xbby)\cos(qL)(\cos\sigma\sin\mu_g + \cos\theta_g\cos\mu_g\sin\sigma));$$

$$F_A = \exp\left(-\frac{(qw)^2}{4}\right)\exp\left(-\frac{1}{2}\left(\frac{l^2}{w^2} - 1\right)(qw)^2\cos^2\mu_g\sin^2\theta_g\right);$$

$$xaay = -\frac{1}{2}(\cos(\mu + \mu_g)\cos\sigma - f_p\sin(\mu + \mu_g)) \times (f_p\cos(\mu + \mu_g) + \cos\sigma\sin(\mu + \mu_g));$$

$$xbby = -\frac{1}{2}(\cos(\mu + \mu_g)\cos\sigma + f_m\sin(\mu + \mu_g)) \times (f_m\cos(\mu + \mu_g) - \cos\sigma\sin(\mu + \mu_g));$$

$$f_p = \sin\theta_g + \cos\theta_g\sin\sigma;$$

$$f_m = \sin\theta_g - \cos\theta_g\sin\sigma \quad (18)$$

Spatial Symmetry of Scattering Patterns

The μ dependence of the scattered power is explicit in the *xaay* and *xbby* terms. Since these terms appear to the second degree, the harmonic expansion in μ will contain constant and

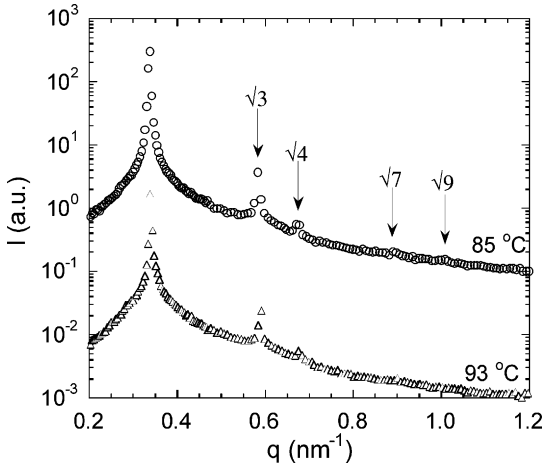

Figure 3. SAXS profiles of SI(7−23) obtained in separate experiments after quiescent ordering from the disordered state at 85 (shifted for clarity) and 93 °C. The relative positions of the higher order scattering peaks corresponding to hexagonally packed cylinders are indicated by arrows and labeled on the profile.

4μ terms. If we change μ to -μ and make the following changes in the integration variables: $\mu_g \rightarrow -\mu_g$, $\sigma \rightarrow \sigma + \pi$, $\theta_g \rightarrow \pi - \theta_g$, we get the same expression for the intensity, so it is even in μ and has the following form:

$$\text{Intensity} = \alpha(\theta) + \beta(\theta)\cos 4\mu \qquad (19)$$

Reduction to 2-Dimensional Integration

The above expression for the intensity involves a 3-dimensional integral over the angle variables $\{\theta_g, \mu_g, \sigma\}$. Numerical evaluations in this form are relatively lengthy in computational time. Using the Fourier Bessel integral, we can transform the expression to terms involving at most 2-dimensional integrals.[28] These can be evaluated numerically in much shorter times and make practical the use of algorithms to obtain optimum matching of theoretical parameters to experimental data. The explicit form of the reduced expressions is given in Appendix 1.[46]

Experimental Details

A polystyrene−polyisoprene diblock copolymer was synthesized by anionic polymerization under high vacuum. The weight-averaged molecular weights of both polystyrene and polyisoprene blocks were determined to be 7.3 and 22.6 kg/mol respectively, and we refer to this polymer as SI(7−23). The volume fraction of the polystyrene block in SI(7−23), f_{PS}, is 0.217. Our synthesis and characterization procedures are given in ref 47. Quiescent birefringence measurements were used to determine that the order−disorder transition temperature of our system was 98 ± 2 °C. The sample was heated above T_{ODT} in the SAXS instrument (beamline 8-ID-I, Advanced Photon Source, Argonne National Laboratory) and cooled to 85 and 93 °C in separate experiments. The SAXS data thus obtained are shown in Figure 3. At both temperatures we observe standard SAXS signatures of a hexagonal phase (higher order scattering peaks at $\sqrt{3}$ and $\sqrt{4}$).

For the transmission electron microscopy (TEM) experiments, two SI(7−23) melt samples were quiescently ordered at 85 and 93 °C for 72 h (after disordering) and rapidly quenched to room temperature. The samples were sectioned using a Leica Ultracut UCT microtome equipped with a Leica EM FCS cryogenic sample chamber operated at −110 °C. The sections 50 nm in thickness were collected on TEM grids and stained 4 h in OsO4 vapor, rendering the diene blocks dark by mass-thickness contrast. A JEOL 100CX TEM, operated at an accelerating voltage of 100 kV, was used to image the stained sections. Typical micrographs obtained from these experiments are shown in Figure 4. We see both hexagonally packed circles and straight lines indicating the presence of ordered polystyrene cylinders.

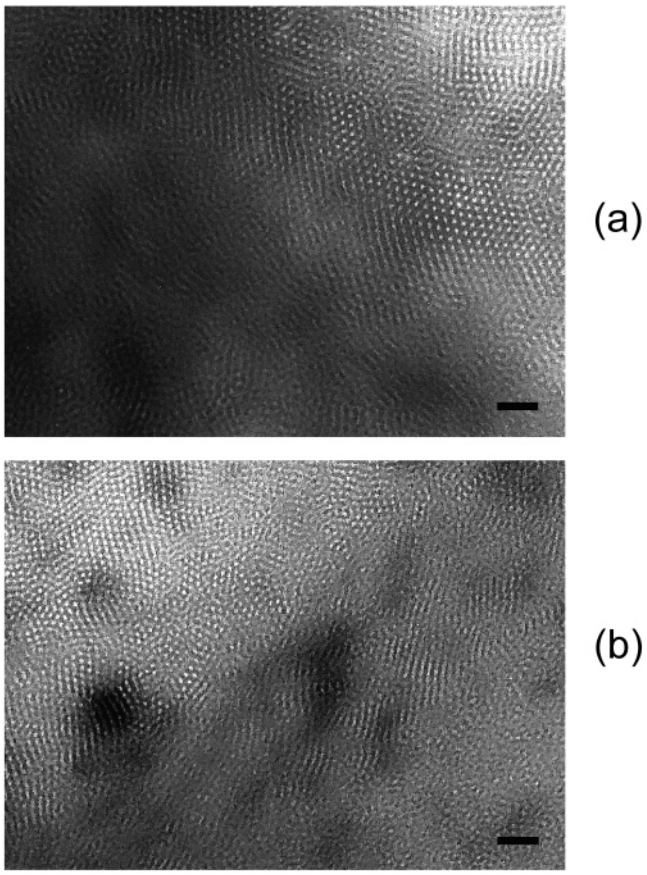

Figure 4. Typical TEM micrographs of SI(7−23) obtained in separate experiments after quiescent ordering from the disordered state at (a) 85 and (b) 93 °C. OsO_4 is used to stain the polyisoprene phase. The length of the scale bar is 100 nm.

The optical properties of our sample, under quiescent conditions and under reciprocating shear flow, were studied using an apparatus described in ref 29. Several 1 mm thick SI(7−23) melts were first heated to 108 °C for 90 min to erase the effect of thermal history. The samples, placed between two crossed polarizers, were then tempered at different temperatures (i.e., 70, 80, 85, 87, 89, 91, 93, and 95°C). It took less than 15 min for each sample to reach its final annealing temperature after the start of cooling. Time zero is defined as the time when the cooling was initiated. Depolarized light scattering patterns and birefringence data were acquired periodically over time, using a HeNe laser (633 nm wavelength) as the light source. Reciprocating shear studies were performed on SI(7−23), using strain amplitudes of 20 and 200% and shear velocities of 0.1 and 1 mm/s. Once again, samples were first disordered under quiescent conditions at 108 °C prior to each shear flow experiment. Shear flow was started immediately at the beginning of the cooling.

Polarized optical microscopy (POM) images were captured 24 h after 100 μm-thick SI(7−23) melts were quenched quiescently from 108 to 85 °C and from 108 to 93 °C, using a hot stage.

Processing of Depolarized Light Scattering Data

Experimentally obtained DPLS patterns in the form of TIFF files were processed by (1) subtracting a background pattern (pattern at time zero), (2) eliminating the central peak (due to incident laser leakage through the crossed polarizers) by truncating the high-intensity values at small scattering angles ($q < 0.04-0.06\ \mu m^{-1}$), (3) removing any secondary reflections by replacing pixels with ones lying at symmetric positions on the other side of the x-axis, (4) cropping the pattern so that the

frame is square, (5) filtering out high spatial frequencies to eliminate extraneous detail and reduce resolution to allow faster numerical analysis, and (6) converting the rectangular coordinates of the scattering direction to polar coordinates, so that rectangular pixels are replaced by annular sectors. The mean value of an annular sector, $M(q, \Delta q, \mu, \Delta\mu)$, is the mean value of the intensity of pixels within the sector $\{q, q + \Delta q\}$, $\{\mu, \mu + \Delta\mu\}$. The nth cosine moment, $f_n(q)$, of M is given by

$$f_n(q) = \Delta\mu\Delta q \int_0^{2\pi} M(q, \Delta q, \mu, \Delta\mu) \cos(n\mu)\, d\mu \quad (20)$$

As discussed above, the theoretical scattered depolarized intensity has the form $f_0(q) + f_4(q) \cos 4\mu$. By calculating cosine moments, we can fit the experimental scattering data directly to this form, making use of scattering data at all azimuthal angles rather than our earlier method which made use of data from only specific values of μ (integer multiples of 45°).

Because any experimental intensity distribution, $I(q,\mu)$, is periodic in μ, it can be expanded in a Fourier series, $\Sigma f_n(q) \cos(n\mu) + \Sigma g_n(q) \sin(n\mu)$. We have calculated both the cosine and sine moments, $f_n(q)$ and $g_n(q)$, for our scattering data for values of n up to 6, and find that all the moments are negligible (maximum value less than ~1.5% of the maximum value of f_0) except for f_0, f_4, and occasionally f_1 and g_1. The f_1 and g_1 moments are sensitive to the choice of the center point of the scattering pattern, and they are sometimes nonnegligible because of a subtle asymmetry in the pattern that is not even detectable by eye. We thus find that the expression $f_0 + f_4 \cos(4\mu)$ constitutes an essentially complete description of the q and μ dependence of our quiescent scattering data.

Comparison of Theory and Experiment

The two-grain model described above was used to calculate a set of normalized moment curves, $f_n^{\text{theory}}(wq)$, for various values of l/w. A linear least squares procedure was used to determine the best fitting values of w, l/w, and an amplitude factor, A, for a given experimental set of cosine moments, $f_n^{\text{expt}}(q)$. For each trial value, w_{trial}, the theoretical abscissa was multiplied by w_{trial}^{-1}, to allow comparison with experiment. For a given nth cosine moment curve consisting of N_n points, the rms deviation is given by

$$\text{dev}(n) = \frac{1}{N_n}\sqrt{\sum_{i=1}^{N_n} [f_n^{\text{expt}}(q_i) - A f_n^{\text{theory}}(q_i)]^2} \quad (21)$$

The final discriminant is formed by the weighted sum of the deviations. For matches involving f_0 and f_4, the discriminant is wt(0)dev(0) + wt(4)dev(4), where

$$\text{wt}(n) = 1/\sum_{i=1}^{N_n} f_n^{\text{expt}}(q_i) \quad (22)$$

Using the *Mathematica* function NMinimize, the best values of the parameters w_{trial}, l/w, and A are determined.

Results and Discussion

The SAXS and TEM results in Figures 3 and 4 indicate the presence of hexagonally packed cylinders in weakly ordered SI(7−23) melts. The results from SI(7−23) thus far are not surprising and in agreement with previous studies on SI diblock copolymers with $f_{PS} \approx 0.22$.[48] The DPLS patterns from SI(7−23) annealed at 85 and 93 °C are shown in parts a and b of Figure 5, respectively. In Figure 5a, we see the development of a plus (+) pattern, where the lobes of the pattern are parallel to the polarizer/analyzer axes, where in Figure 5b we see the usual cross (X) pattern associated with randomly oriented anisotropic granular structures developed in block copolymers.[7,8,25−29,48−52] We followed the development of these depolarized light scattering patterns at different annealing temperatures ranging from 70 to 95 °C. At shallow quench depths (T > 88 °C), we observed cross (X) depolarized scattering patterns, in which the four scattering lobes are at 45° to the polarizer-analyzer axes. In contrast, at deep quench depths (T < 88 °C), we observed plus (+) depolarized scattering patterns. The fact that we observe different scattering patterns at different annealing temperatures is not surprising, since defect structures in block copolymers are sensitive functions of quench depth.[50] On the other hand, a plus scattering pattern has never been a signature of block copolymer scattering. We also noticed that the cross and plus patterns were not interconvertible upon changing the annealing temperature nor do they disappear after long annealing, indicating that once formed, there are large free energy barriers that prevent conversion of one defect type to the other. All the observed scattering patterns, whether cross or plus, decreased in size and became more intense as a function of time, indicating that the size and volume fraction of the scattering domains increase with increasing time.

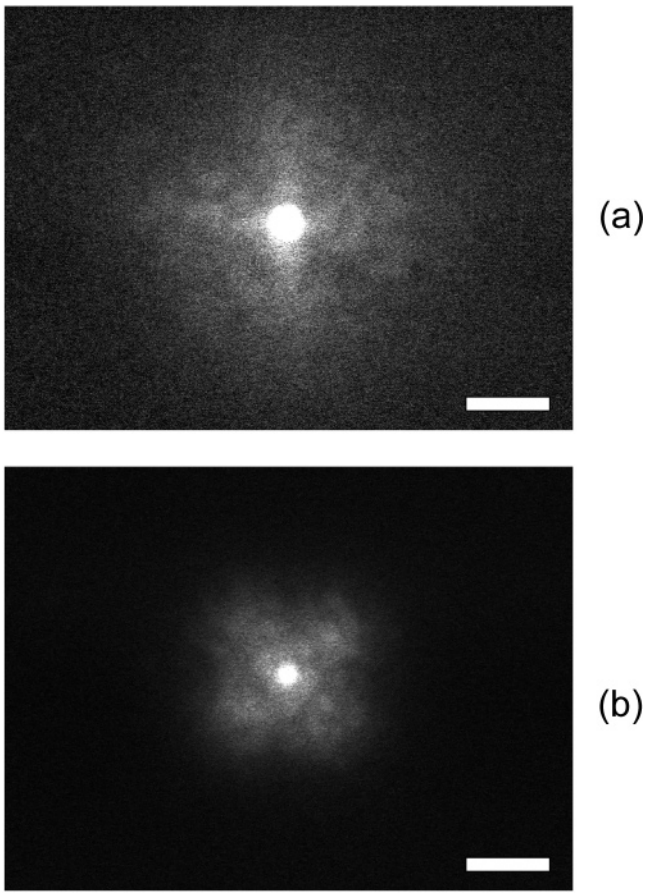

Figure 5. DPLS patterns for SI(7−23): (a) plus pattern of the sample annealed at 85 °C after 86 h of annealing; (b) cross pattern of the sample annealed at 93 °C after 1 h of annealing. The length of the scale bar corresponds to a difference in q of 0.20 μm^{-1}.

The corresponding cosine moments, $f_0(q)$ and $f_4(q)$, obtained from the two images shown in Figure 5, parts a and b, are also qualitatively different and are shown respectively in parts a and b of Figure 6. In Figure 6a, $f_4(q) > 0$ for all q, because the

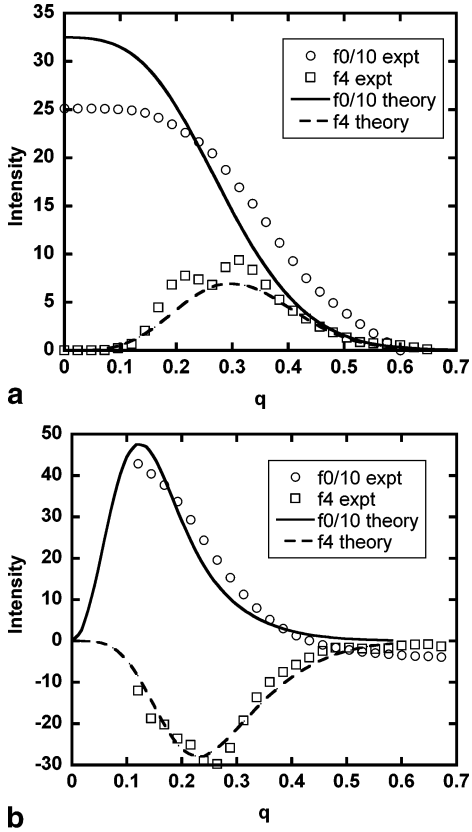

Figure 6. Cosine moments, $f_0(q)$ and $f_4(q)$ for SI(7−23). Parts a and b correspond to parts a and b in Figure 5, respectively. Symbols represent experimental data points, while lines represent theoretical fits. $f_0(q)$ is divided by 10 to show both $f_0(q)$ and $f_4(q)$ on the same plot. Units of q are μm^{-1}. Units of intensity are arbitrary, but they are the same for parts a and b.

scattered intensity along $\mu = 0°$ is larger than that along $\mu = 45°$, whereas in Figure 6b, $f_4(q) < 0$ for all q, because the scattered intensity along $\mu = 45°$ is larger than that along $\mu = 0°$.

The curves in Figure 6 are least-squares theoretical fits through the experimental data. The best fit of the data in Figure 6a to the 2-grain theory, obtained for $l/w = 3$, $w = 4.42$ μm and $L/w = 2$, clearly captures all of the important experimental features in the $f_0(q)$ and $f_4(q)$ data. The data in Figure 6b are similar to data published in ref 28. As in ref 28, we used the twisted-H 3-grain model to analyze the data. In this model, the sample is composed of randomly oriented clusters of three anisotropic grains with characteristic lengths l and w, wherein each grain is described by a Gaussian shape function, and Δ is a parameter that describes the polydispersity of grain sizes. The theoretical curves in Figure 6b correspond to $l/w = 3$, $w = 5.15$ μm, and $\Delta = 0$. It is evident that the length scale of local correlations in the nematic texture (Figure 6a) is similar to those obtained from block copolymers with a granular defect structure (Figure 6b).

Birefringence data, i.e., the fraction of incident light transmitted through crossed polarizers P/P_0, were collected as a function of time, for the SI(7−23) samples annealed quiescently at 85, 87, 89, 91, and 93 °C (see Figure 7). The results suggest two different ordering mechanisms depending on the quench depth. In the vicinity of the sample's order−disorder transition temperature (at $T > 88$ °C), the ordering process proceeds by classical nucleation and growth as we can see from the *S*-shaped profiles indicating an induction period (nucleation) followed by a fast growth period (grain growth), followed by a slow growth

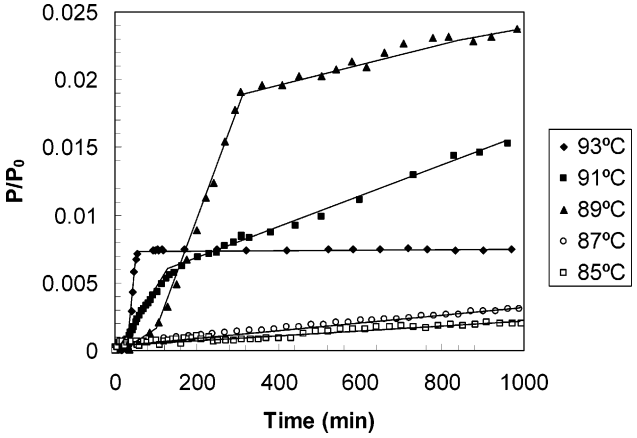

Figure 7. Time dependence birefringence measurements for the SI-(7−23) samples annealed quiescently at different temperatures.

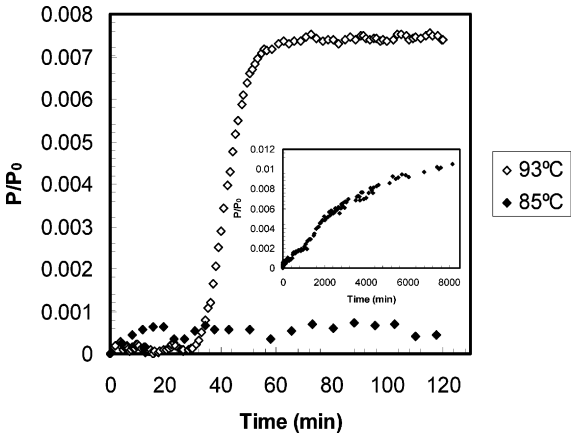

Figure 8. Birefringence profiles for the samples annealed quiescently at 85 and 93 °C. The inset shows the birefringence profile for the 85 °C sample over 8000 min.

period (defect annihilation). At large quench depths (at $T < 88$ °C), we do not see the same distinct kinetic periods that we have seen at shallow quench depths. To allow for a better comparison between the two ordering mechanisms, we focus on the early time birefringence signal obtained at 85 and at 93 °C in Figure 8. To confirm the qualitative difference between the two ordering regimes, we monitored the birefringence signal at 85 °C for well over 8000 min, as shown in the inset of Figure 8. No evidence of distinct ordering kinetics regimes is seen at 85 °C. The time dependence of the order formation seen at temperatures below 88 °C may be a signature of spinodal decomposition,[52] or it may be the result of nonequilibrium effects owing to very high nucleation density.[50]

The time dependence of the birefringence, obtained after quenching SI(7−23) from 108 to 85 °C and from 108 to 93 °C, under reciprocating shear flow (200% strain amplitude and 1 mm/s shear velocity), is shown in Figure 9. At 85 °C, we find that P/P_0 increases rapidly to unity, and then levels off at $t = 15$ min ($t = 0$ is defined as the time when both the cooling and the shearing were started). At 93 °C, it took about 120 min for the birefringence signal to level off at $P/P_0 \approx 0.7$. By comparing the kinetic profiles at 85 and 93 °C under both quiescent (see Figure 8) and shear flow (see Figure 9), we can conclude that shearing the nematic texture, produces excellent and rapid alignment, in sharp contrast to the quiescent results at the same temperature (i.e., 85 °C) where order formation was not complete even after 8000 min of annealing. This in turn can prove to be of great practical importance in future applications using block copolymers.[53]

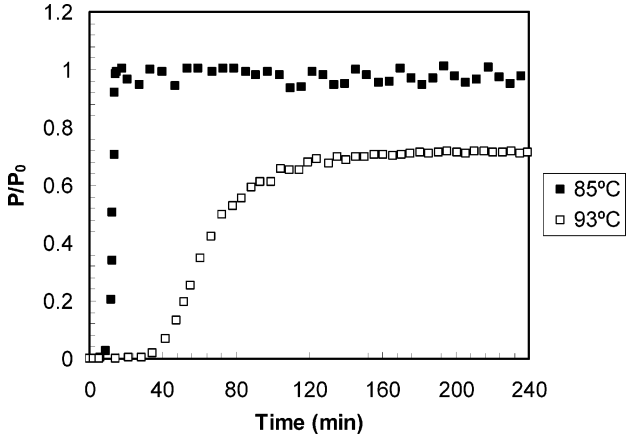

Figure 9. P/P_0 vs time for SI(7−23) annealed under shear flow at selected temperatures (85 and 93 °C).

We also note that there was no measurable depolarized light scattering at finite scattering angles at any time during the (200% strain amplitude) shear flow experiment. On the basis of previous work, we take this as an indication that the fraction of randomly oriented grains is either negligible (i.e., formation of a perfect single crystal)[29] or that these grains are nearly parallel to the flow direction.[30] On the other hand, when relatively low-strain amplitude was used (20%), we observed measurable depolarized light scattering patterns at finite scattering angles similar to those obtained in the quiescent experiments (i.e., plus patterns at 85 °C and cross patterns at 93 °C). The developed scattering patterns did not disappear or interchange at any point during the (low-strain) experiments, indicating that these developing defect structures are in fact kinetically stable not only under quiescent but also under mild strain conditions.

In POM, the visualization of the ordered texture of a sample held between two crossed polarizers, depends very much on the film thickness. When the thickness of a sample is much larger than the domain (grain) size, the optical texture becomes very blurred, and it consists of only unshaped bright and dark regions due to the overlay of the textures along the thickness direction. When the thickness of a sample is too small, the optical path length becomes too short and the propagating light does not encounter enough ordered structures to cause these weakly birefringent materials to have sufficient visual contrast, which means that the optical textures would be invisible (dark) under the microscope. Parts a and b of Figure 10 shows images taken 24 h after two 100-μm-thick SI(7−23) melts were quenched quiescently from 108 to 85 °C and from 108 to 93 °C respectively, using a hot stage. The texture obtained at 85 °C, shown in Figure 10a, reveals a continuous and smooth change of the director, and is very similar to POM images obtained from liquid crystalline polymers and other nematic fluids. The large sampling area in Figure 10a along with depolarized light scattering data shown in Figure 5a indicate that the observed nematic texture is a global feature of our SI(7−23) block copolymer sample. Given the thickness of the samples used in the optical characterization of these systems, we conclude that these micrometer-sized nematic defects are 3D structures where the directors continuously change their orientation and that there are no grain boundary walls where the directors discontinuously change their orientation. POM images obtained at 93 °C, shown in Figure 10b, are devoid of nematic texture.

We have thus shown that the nature of coherent order in SI(7−23) melts depends crucially on the annealing temperature. Annealing the sample at 93 °C leads to the formation of

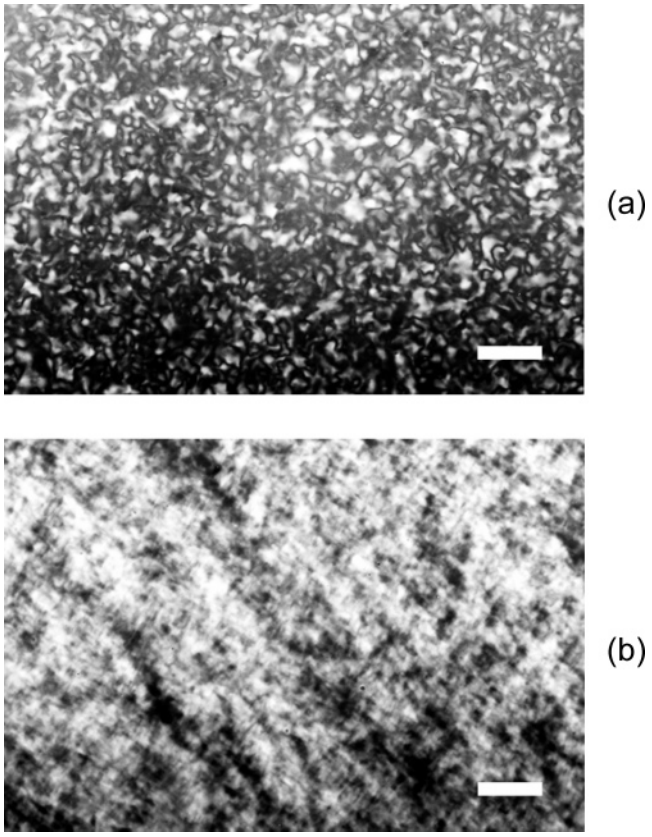

Figure 10. Polarized optical microscopy images taken after 24 h for 100 μm samples annealed quiescently: (a) 85 °C showing nematic texture; (b) 93 °C showing granular structure. The length of the scale bar is 50 μm.

randomly oriented grains, while annealing the sample at 85 °C leads to the development of nematic texture. The difference in the coherent order can only be detected in experiments that probe the local structure on the micrometer length scale, i.e., DPLS and POM. We also show that the shear alignment characteristics of the granular and nematic phase are very different. However, experiments that probe the nature of coherent order on the nanometer length scale such as SAXS and TEM show no dependence of structure on annealing temperature.

The unique optic axis of the cylinder phase of block copolymers is aligned along the cylinder axis. We thus conclude that the nematic director (see Figure 1a) in SI(7−23) is coincident with the local orientation of bundles of hexagonally packed cylinders. The reason for obtaining a nematic phase in SI(7−23) is not entirely clear at this point. The characteristic coherence length of the structures obtained at 93 °C ($l/w = 3$, $w = 5.15$ μm) and 85 °C ($l/w = 3$, $w = 4.42$ μm) are similar. There is thus no qualitative difference in the average defect density obtained in the granular and nematic phases. Nematic phases are traditionally formed by stiff rodlike molecules. One might thus conclude that the stiffness of the glassy polystyrene cylinders may be responsible for the formation of the nematic phase in SI(7−23). It may be noted that our annealing temperature of 85 °C is close to the glass transition of a 7 kg/mol homopolystyrene melt. We have studied a series of SI block copolymers with cylindrical morphologies in refs 26−28 and 49, and the nematic phase was not observed in those experiments despite the proximity of the annealing temperature to the glass transition temperature of the polystyrene phase.

We propose that the formation of the nematic phase is related to the composition of the block copolymer. In ref 48 we studied grain growth in SI(7−26) with $f = 0.18$ while in refs 28 and

50 we studied grain growth in SI(4−13) and SI(20−6) with $f = 0.23$ and $f = 0.26$, respectively. (In our nomenclature, the numbers in brackets are an ordered pair, representing the molecular weights of the polystyrene and polyisoprene blocks in kg/mol and f is the volume fraction of the minor component.) All of these copolymers are weakly ordered with accessible order−disorder transitions. The grain structure in both SI(4−13) and SI(20−6) could be described by relatively simple grain models wherein the optic axis was assumed to be constant within individual grains. In SI(7−26), however, we were unable to detect any signs of coherent order on the micrometer length scale after quiescent annealing, regardless of annealing temperature.[49] The SAXS patterns of SI(7−26) were, however, very similar to those shown here for SI(7−23). We concluded in ref 48 that $f = 0.18$ is at the border between cylinders and the body centered cubic phase of block copolymers, and the thermodynamic driving force needed to obtain micrometer-sized coherent domains of a hexagonal phase was absent. Despite this, we reported in ref 48 that the application of shear flow to SI(7−26) led to rapid development of a well-ordered single crystal. In this regard, SI(7−26) shows alignment behavior that is similar to that seen in the nematic phase of SI(7−23). We recognized that the present sample SI(7−23) with $f = 0.21$ lies between $f = 0.18$ where we see no long range order and $f = 0.23$ where we obtain a simple collection of coherent grains. We thus suggest that the driving force of obtaining coherently ordered grains in cylindrical block copolymers decreases monotonically with decreasing f, as the sphere−cylinder border is approached. Very close to this border, there is no coherent order on the micrometer length scale. As f is increased, one obtains coherent order on micrometer length scales but the local director changes direction continuously, leading to the presence of disclinations. Ellipsoidal grains with a well-defined director are only obtained when $f \geq 0.23$ or when the sample is annealed sufficiently close to the order−disorder transition temperature. Our proposal regarding the relationship between grain structure and block copolymer composition is based on a limited sample set covering a few discrete values of f. A more systematic study of the dependence of grain structure on f seems warranted.

Concluding Remarks

We have observed depolarized light scattering (DPLS) patterns with 4-fold symmetry where the lobes of the patterns are oriented along the polarizer/analyzer axes (plus patterns) from a cylindrical polystyrene−polyisoprene diblock copolymer melt SI(7−23), quenched from the disordered state and annealed at relatively large quench depths ($T < 88$ °C). However, when the same sample was annealed at small quench depths ($T > 88$ °C) the lobes were oriented at the usual ±45° directions relative to the polarizer/analyzer axes.

The ordering kinetics of these samples was investigated by time-resolved optical birefringence. The results suggest two different ordering mechanisms depending on the quench depth. Polarized optical microscopy (POM) images confirmed the formation of micrometer-sized coherent regions with defects similar to the nematic (Schlieren) textures seen in other liquid crystalline materials. The nematic textures appeared only at deep quenches. At shallow quenches the usual granular structures were seen by POM, which is consistent with our depolarized light scattering observations. The sampling size and the thickness of the samples used in the POM experiments along with the DPLS data indicate that these novel defect structures (i.e., nematic textures) are present throughout the sample, and not just localized in certain positions within the sample. The fact that this texture grows with time and does not disappear upon prolonged annealing, changing thermal conditions, and/or mild shearing indicates that it is kinetically stable. Finally, shearing the nematic texture with a high-strain amplitude produces rapid and excellent alignment while shearing granular samples does not. This is important for future applications where aligned block copolymer phases are needed.

Acknowledgment. Financial support provided by the National Science Foundation (Grant DMR-0213508 and DMR-0514422) is gratefully acknowledged. The Advanced Photon Source and Argonne National Laboratory is supported by DOE under contract number W-31-109-Eng-38. The TEM work was supported by the Army Research Office Polymer Chemistry Program (W911NF-04-1-0329). This manuscript was significantly improved due to the critical comments of the reviewers.

Appendix 1: Expressions for 2-Dimensional Integration

The average scattered intensity from a statistical ensemble of AB grain pairs can be calculated from the following expressions, which involve a 2-dimensional integration over angles θ_g and μ_g:[28]

$$I_{AB}(q,\mu) = 2AA + AB \tag{A1}$$

$$AA = 2\pi\exp\left(-\frac{1}{2}(qw)^2\right)\int_0^{\pi} d\theta_g \sin\theta_g \exp(-\zeta)(aaI_0(\zeta) + bbI_2(\zeta)\cos 4\mu) \tag{A2}$$

$$AB = 4\pi\exp\left(-\frac{1}{2}(qw)^2\right)\int_0^{\pi} d\theta_g \sin\theta_g \int_0^{2\pi} d\mu_g \exp(-\zeta(1+\cos 2\mu_g))(J_0(A)(c0 + cCoef0\cos 4\mu_g) + J_2(A)(-(cC2\sigma + cCoefc2\sigma C\cos 4\mu_g))\cos 2\phi + J_4(A)(cC4\sigma + cCoefC4\sigma\cos 4\mu_g)\cos 4\phi) \tag{A3}$$

$$\zeta = \frac{1}{4}(low^2 - 1)(qw)^2\sin^2\theta_g \tag{A4}$$

$$aa = -\frac{1}{1024}\pi(44\cos 2\theta_g + 13\cos 4\theta_g - 121) \tag{A5}$$

$$bb = \frac{13}{128}\pi\sin^4\theta_g \tag{A6}$$

$$A = qwLow\sqrt{\cos^2 2\theta_g \cos^2\mu_g + \sin^2\mu_g} \tag{A7}$$

$$\phi = \tan^{-1}(\sin\mu_g - \cos\theta_g\cos\mu_g) \tag{A8}$$

$$\{c0, cC2\sigma, cC4\sigma\} = \left\{\frac{1}{2048}(84\cos 2\theta_g + 19\cos 4\theta_g - 39), \frac{1}{4096}(160\cos 2\theta_g - 24\cos 4\theta_g - 136), \frac{1}{4096}(-8\cos 2\theta_g + 2\cos 4\theta_g + 6)\right\} \tag{A9}$$

$$\{cCoef0, cCoefC2\sigma, cCoef4\sigma\} = \left\{-\frac{19}{256}\cos(4\mu)\sin^4\theta_g, -\frac{3}{128}(\cos 2\theta_g + 3)\cos 4\mu\sin^2\theta_g, -\frac{1}{2048}(28\cos 2\theta_g + \cos 4\theta_g + 35)\cos 4\mu\right\} \tag{A10}$$

$$low = \text{//}\, w \tag{A11}$$

$$Low = L/w \tag{A12}$$

References and Notes

(1) Bates, F. S.; Fredrickson, G. H. *Annu. Rev. Phys. Chem.* **1990**, *41*, 525.
(2) Leibler, L. *Macromolecules* **1980**, *13*, 1602.

(3) Fredrickson, G. H.; Helfand, E. *J. Chem. Phys.* **1987**, *87*, 697.
(4) Matsen, M. W.; Bates, F. S. *Macromolecules* **1996**, *29*, 1091.
(5) Brazovskii, S. A. *Sov. Phys. JETP* **1975**, *41*, 85.
(6) Gido, S. P.; Gunther, J.; Thomas, E. L.; Hoffman, D. *Macromolecules* **1993**, *26*, 4506.
(7) Garetz, B. A.; Balsara, N. P.; Dai, H. J.; Wang, Z.; Newstein, M. C.; Majumdar, B. *Macromolecules* **1996**, *29*, 4675.
(8) Chang, M. Y.; Abuzaina, F. M.; Kim, W. G.; Garetz, B. A.; Newstein, M. C.; Balsara, N. P.; Yang, L.; Gido, S. P.; Cohen, R. E.; Boontonkong, Y.; Bellare, A. *Macromolecules* **2002**, *35*, 4437.
(9) Sakamoto, N.; Hashimoto, T. *Macromolecules* **1998**, *31*, 8493.
(10) Hashimoto, T.; Sakamoto, N. *Macromolecules* **1995**, *28*, 4779.
(11) Segalman, R. A.; Yokoyama, H.; Kramer, E. J. *Adv. Mater.* **2001**, *13*, 1152, and references therein.
(12) Hahm, J.; Lopes, W. A.; Jaeger, H. M.; Sibener, S. J. *J. Chem. Phys.* **1998**, *109*, 10111.
(13) Harrison, C.; Adamson, D. H.; Cheng, Z.; Sebastian, J. M.; Sethuraman, S.; Huse, D. A.; Register, R. A.; Chaikin, P. M. *Science* **2000**, *290*, 1558.
(14) Harrison, C.; Cheng, Z.; Sethuran, S.; Huse, D.; Chaiken, P. M.; Vega, D. A.; Sebastian, J. M.; Register, R. A.; Adamson, D. H. *Phys. Rev. E* **2002**, *66*, 011706.
(15) Sivaniah, E.; Genzer, J.; Fredrickson, G. H.; Kramer, E. J.; Xiang, M.; Li, X.; Ober, C. K.; Magonov, S. *Langmuir* **2001**, *17*, 4342.
(16) Hammond, M. R.; Cochran, E.; Fredrickson, G. H.; Kramer, E. J. *Macromolecules* **2005**, *38*, 6575.
(17) Heier, J.; Sivaniah, E.; Kramer, E. J. *Macromolecules* **1999**, *32*, 9007.
(18) Kumaki, J.; Hashimoto, T. *J. Am. Chem. Soc.* **2003**, *125*, 4907.
(19) Laurer, J. H.; Fung, J. C.; Sedat, J. W.; Smith, S. D.; Samseth, J.; Mortensen, K.; Agard, D. A.; Spontak, R. J. *Langmuir* **1997**, *13*, 2177.
(20) Jinnai, H.; Kajihara, T.; Watashiba, Y.; Spontak, R. *Phys. Rev. E* **2001**, *64*, 010803 (R).
(21) Laurer, J. H.; Hajduk, D. A.; Fung, J. C.; Sedat, J. W.; Smith, S. D.; Gruner, S. M.; Agard, D. A.; Spontak, R. J. *Macromolecules* **1997**, *30*, 3938.
(22) Chastek, T. Q.; Lodge, T. P. *Macromolecules* **2003**, *36*, 7672.
(23) Chastek, T. Q.; Lodge, T. P. *Macromolecules* **2004**, *37*, 4891.
(24) Balsara, N. P.; Garetz, B. A.; Dai, H. J. *Macromolecules* **1992**, *25*, 6072.
(25) Garetz, B. A.; Newstein, M. C.; Dai, H. J.; Jonnalagadda, S. V.; Balsara, N. P. *Macromolecules* **1993**, *26*, 3151.
(26) Newstein, M. C.; Garetz, B. A.; Dai, H. J.; Balsara, N. P. *Macromolecules* **1995**, *28*, 4587.
(27) Dai, H. J.; Balsara, N. P.; Garetz, B. A.; Newstein, M. C. *Phys. Rev. Lett.* **1996**, *77*, 3677.
(28) Newstein, M. C.; Garetz, B. A.; Balsara, N. P.; Chang, M. Y.; Dai, H. J. *Macromolecules* **1998**, *31*, 64.
(29) Wang, H.; Newstein, M. C.; Chang, M. Y.; Balsara, N. P.; Garetz, B. A. *Macromolecules* **2000**, *33*, 3719.
(30) Abuzaina, F. M.; Garetz, B. A.; Mody, J. U.; Newstein, M. C.; Balsara, N. P. *Macromolecules* **2004**, *37*, 4185−4195.
(31) Demus; D.; Richter, L. *Textures of Liquid Crystals*, Verlag Chemie: Weinheim, Germany, 1978.
(32) Chandrasekhar, S. *Liquid Crystals*, 2nd ed. Cambridge University Press: New York, 1992.
(33) Rojstaczer, S.; Stein, R. S. *Mol. Cryst. Liq. Cryst.* **1988**, *157*, 293.
(34) Wilkes, G. L. *J. Polym., Polym. Lett. Ed.* **1972**, *10*, 935.
(35) Balbontin, G.; Asada, T. Presented at the 33rd IUPAC International Symposium on Macromolecules, Montreal, Canada, 1990.
(36) Rojstaczer, S. R.; Stein, R. S. *Macromolecules* **1990**, *23*, 4863.
(37) Silvestri, R.; Chapoy, L. L. *Polymer* **1992**, *33*, 2891.
(38) Hashimoto, T.; Nakai, A.; Shiwaku, T.; Hasegawa, H.; Rojstaczer, S.; Stein, R. S. *Macromolecules* **1989**, *22*, 422.
(39) Shiwaku, T.; Nakai, A.; Hasegawa, H.; Hashimoto, T. *Macromolecules* **1990**, *23*, 1590.
(40) Peiffer, D. G. *Polymer* **1991**, *32*, 134.
(41) Wang, W.; Hashimoto, T. *Macromolecules* **1999**, *33*, 2891.
(42) Wang, W.; Hashimoto, T. *Polymer* **2000**, *41*, 4729.
(43) Winey, K. I.; Patel, S. S.; Larson, R. G.; Watanabe, H. *Macromolecules* **1993**, *26*, 2542.
(44) Amundson, K.; Helfand, E.; Quan, X.; Hudson, S. D.; Smith, S. D. *Macromolecules* **1994**, *27*, 6559.
(45) Greco, F. *Macromolecules* **1989**, *22*, 5719.
(46) Details of the derivation and *Mathematica* programs used for the generation of the curves are available from the authors upon request.
(47) Lin, C. C.; Jonnalagadda, S. V.; Kesani, P. K.; Dai, H. J.; Balsara, N. P. *Macromolecules* **1994**, *27*, 7769.
(48) Abuzaina, F. M.; Patel, A. J.; Mochrie, S.; Narayanan, S.; Sandy, A.; Garetz, B. A.; Balsara, N. P. *Macromolecules* **2005**, *38*, 7090.
(49) Chastek, T. Q.; Lodge, T. P. *Macromolecules* **2004**, *37*, 4891.
(50) Kim, G. W.; Chang, M. Y.; Garetz, B. A.; Newstein, M. C.; Balsara, N. P.; Lee, J. H.; Hahn, H.; Patel, S. S. *J. Chem. Phys.* **2001**, *114*, 10196.
(51) Newstein, M. C.; Balsara, N. P.; Garetz, B. A.; Chang, M. Y.; Dai, H. J.; Goveas, J. L.; Krishnamoorti, R. *Macromolecules* **1998**, *31*, 5309.
(52) Newstein, M. C.; Balsara, N. P.; Garetz, B. A.; Bauer, B. J.; Prosa, T. J. *Macromolecules* **1998**, *31*, 7668.
(53) Balsara, N. P.; Dai, H. J.; Kesani, P. K.; Garetz, B. A.; Hammouda, B. *Macromolecules* **1994**, *27*, 7406.
(54) Lodge, T. P. *Macromol. Chem. Phys.* **2003**, *204*, 265.

MA052413W